DOI: 10.1002/zaac.200800116

The Metallic Zintl Phase Ba_3Si_4 – Synthesis, Crystal Structure, Chemical Bonding, and Physical Properties

Umut Aydemir[a], Alim Ormeci[a], Horst Borrmann[a], Bodo Böhme[a], Fabio Zürcher[b], Burcu Uslu[d], Thorsten Goebel[a], Walter Schnelle[a], Paul Simon[a], Wilder Carrillo-Cabrera[a], Frank Haarmann[a], Michael Baitinger[a], Reinhard Nesper[b], Hans Georg von Schnering[c], and Yuri Grin[a,*]

[a] Dresden, Max-Planck-Institut für Chemische Physik fester Stoffe
[b] Zürich / Switzerland, ETH, Laboratorium für Anorganische Chemie
[c] Stuttgart, Max-Planck-Institut für Festkörperforschung
[d] Istanbul / Turkey, Koç University, Chemistry Department

Received March 26th, 2008.

Abstract. The Zintl phase Ba_3Si_4 has been synthesized from the elements at 1273 K as a single phase. No homogeneity range has been found. The compound decomposes peritectically at 1307(5) K to $BaSi_2$ and melt. The butterfly-shaped Si_4^{6-} Zintl anion in the crystal structure of Ba_3Si_4 (Pearson symbol *tP*28, space group $P4_2/mnm$, a = 8.5233(3) Å, c = 11.8322(6) Å) shows only slightly different Si-Si bond lengths of d(Si−Si) = 2.4183(6) Å (1×) and 2.4254(3) Å (4×). The compound is diamagnetic with $\chi \approx -50 \times 10^{-6}$ cm^3 mol^{-1}. DC resistivity measurements show a high electrical resistivity (ρ(300 K) $\approx 1.2 \times 10^{-3}$ Ω m) with positive temperature gradient dρ/dT. The temperature dependence of the isotropic signal shift and the spin-lattice relaxation times in ^{29}Si NMR spectroscopy confirms the metallic behavior. The experimental results are in accordance with the calculated electronic band structure, which indicates a metal with a low density of states at the Fermi level. The electron localization function (ELF) is used for analysis of chemical bonding. The reaction of solid Ba_3Si_4 with gaseous HCl leads to the oxidation of the Si_4^{6-} Zintl anion and yields nanoporous silicon.

Keywords: Barium; Tribariumtetrasilicide; Zintl phases; Phase diagrams; Electronic structure; Chemical bonding; Nanoporous silicon; Crystal structures

1 Introduction

Intermetallic compounds of alkali metals and earth alkali metals with group 14 elements form crystal structures with a broad variety of polyanions with covalent bonds, which follow the Zintl-Klemm concept [1]. Numerous crystal structures of Zintl phases were determined, but only little is known about their physical properties due to their high reactivity against oxygen and moisture. It is expected that Zintl phases of closed shell cations and polyanions should be in general diamagnetic semiconductors. However, atomic interactions in solid phases influence the electronic structure, which may result in a nonzero density of states (DOS) at the Fermi energy E_F [2, 3]. Therefore, more precise predictions of physical properties need quantum mechanical calculations as demonstrated, e.g., by the unexpected metallic behavior of single phase Ba_3Si_4. This compound contains quasi-isolated Si_4^{6-} anion, as first reported in 1969 by *Eisenmann* et al. [4]. The butterfly shaped anion was explained with the formal charge distribution $[Ba^{2+}]_3[(3b)Si^{1-}]_2[(2b)Si^{2-}]_2$, being in agreement with the Zintl concept [4, 5]. Investigations on the oxidation behavior of binary compounds with alkali metals and main group elements led to the preparation of new phases with framework structures [6–8]. The extension of these studies to the compounds of alkaline earth metals was the next logical step, thus attracting our attention to Ba_3Si_4.

In the present study, the crystal structure was re-determined to higher accuracy. The binary system Ba–Si was reinvestigated in the range of 50–60 at-% Si and the synthesis of Ba_3Si_4 was optimized. Electrical and magnetic properties were measured on single-phase samples and compared with the results of quantum mechanical calculations. The electronic transport properties were confirmed by extensive ^{29}Si NMR spectroscopy experiments, which are independent from grain boundaries and contact problems. Finally, the chemical reactivity of Ba_3Si_4 and its reaction with gaseous HCl were investigated.

2 Experimental Details

2.1 Preparation

Ba_3Si_4 – 0.7858 g (5.7 mmol) Ba (ChemPur, 99.9 %) and 0.2143 g (7.6 mmol) Si (ChemPur, 99.999 %) were sealed under argon in a Ta container. The container was further fused under argon in a silica ampoule and placed vertically in a tube furnace. In the first

* Prof. Dr. Yu. Grin
Max-Planck-Institut für Chemische Physik fester Stoffe
Nöthnitzer Straße 40
01187 Dresden/Germany
E-mail: grin@cpfs.mpg.de
Fax: +049-351-4646-4002

step of the reaction, the sample was heated in 3 hours to 1473 K, annealed for 1 h at this temperature, and then quenched to room temperature. Alternatively, induction heating was used as the first step. The heating was performed slowly enough to prevent the evaporation of Ba. In the second step, the sample was annealed for 3 days at 1273 K. The reaction product consists of metallic shining, brittle, well-shaped crystals and is a single phase according to XRPD and SEM (Fig. 1). It is very sensitive to air and moisture; therefore all sample manipulations were carried out in an argon-filled glove box. EDXS analysis on three different pieces revealed the chemical composition $Ba_{3.0(1)}Si_{4.1(1)}$. A reaction under same conditions in open glassy carbon crucibles, welded in tantalum ampoules, lead always to the formation of small amounts of $BaSi_2$ as a by-product. Evaporation of Ba was not observed at this temperature.

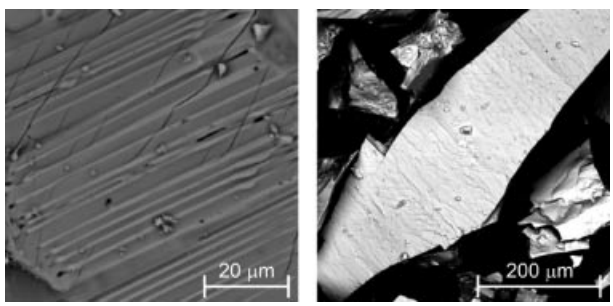

Fig. 1 SEM images of Ba_3Si_4. The lamellar structure is an indication of the formation from the melt. The sample is homogeneous according to EDXS.

$Ba_3{}^{29}Si_4$: A sample for NMR experiments was synthesized with the same reaction conditions from 98.70 % enriched ^{29}Si (Isoflex). No silicon-containing impurity phases were detected in the ^{29}Si NMR experiment. XRPD shows single-phase Ba_3Si_4.

BaSi: 0.8302 g (6.05 mmol) Ba and 0.1698 g (6.05 mmol) Si were sealed under argon in a Ta ampoule. The sample was heated in 24 h to 1473 K and then annealed for 2 h at this temperature. The ampoule was quenched in water to room temperature and then annealed for 3 more days at 1073 K. The reaction product is metallic shining, brittle, and very sensitive to air and moisture. XRPD did not show any by-products.

$BaSi_2$: 0.7097 g (5.17 mmol) Ba and 0.2903 g (10.34 mmol) Si were placed in a glassy carbon crucible. The sample was melted under argon with an induction furnace and cooled down within few minutes to room temperature. No Ba evaporation was observed. The fine crystalline powder is sensitive to air and moisture and did not contain any by-product according to XRPD. Larger crystals were obtained by subsequent annealing at 1273 K for 2 d.

Nanoporous silicon: Fine powder of Ba_3Si_4 (13 mg, 0.025 mmol) and dry NH_4Cl (40 mg, 0.75 mmol) were placed into separate aluminum oxide crucibles and were sealed together into a quartz ampoule under Ar atmosphere. Subsequently, the ampoule was annealed in a tube furnace at 873 K for 2.5 hours. XRPD of the reaction product shows the reflections of $BaCl_2$. The product was washed with distilled water to dissolve $BaCl_2$. Brownish powder was obtained which is amorphous according to XRPD. All particles which were investigated by EDXS with high-resolution SEM consist only of silicon. According to EDXS the overall sample contains less than 1 wt-% Ba.

Table 1 Crystallographic data of Ba_3Si_4.

Formula; molar mass	Ba_3Si_4; 524.323 g mol^{-1}
Crystal system; space group	tetragonal; $P4_2/mnm$ (no. 136)
a / Å; c / Å	8.5233(3); 11.8322(6)
Unit cell volume	859.57(6) Å^3
Z; ρ_{calc}/(g cm^{-3})	4; 4.0516(3)
Diffractometer	RIGAKU Spider
Wave length λ / Å; monochromator	0.56087; multilayer-optics
Crystal size	40 × 50 × 70 µm
T / K	295
θ range	2.67° to 40.00°
Indexes ranges	$-19 \le h \le 13$, $-18 \le k \le 10$, $-26 \le l \le 20$
μ / mm^{-1}	7.424
$F(000)$ / e	896
Absorption correction	Multi-scan
Reflections collected; independent	24327; 2931 [R_{int} = 0.017]
Refinement method	Full-matrix least-squares on F^2
Refined parameters	24
Residuals [I > 2σ(I)]	$R1$ = 0.015, $wR2$ = 0.023
Residuals (all data)	$R1$ = 0.021, $wR2$ = 0.024
Goodness-of-fit on F^2	1.212
Extinction coefficient	0.00471(12)
Largest diff. peak and hole	1.372 and −0.973 e / Å^3

2.2 Characterization

X-Ray powder diffraction: The samples were finely ground under argon in an agate mortar and placed on a sample holder between two polyimide X-Ray films (d = 7.5 µm, Chemplex). The X-ray films were sealed with vacuum grease (Lithelen, Leybold), which protected the samples from oxidation during the measurement. Phase analysis on powder was performed with X-ray Guinier diffraction technique (Huber G670 camera, Cu $K\alpha_1$ radiation, λ = 1.540598 Å, graphite monochromator, 5° ≤ 2θ ≤ 100°, $\Delta 2\theta$ = 0.005°, LaB_6, NIST standard, a = 4.1569162(97) Å at 295.5 K). The reflection positions were determined by a single profile fit and the unit cell parameters were calculated from a least-square refinement [9].

X-ray single crystal diffraction: Single crystals were selected from the sample under argon and sealed in Mark-tubes (borosilicate glass, ∅ = 0.2 mm, d = 0.01 mm, Hilgenberg). The measurements were performed with a rotating anode diffractometer (RIGAKU Spider, Varimax optical system, Ag $K\alpha$ radiation λ = 0.56087 Å). Absorption correction was performed with a multi-scan procedure and the crystal structure refinement by employing a full-matrix least-squares procedure [10]. Details concerning the data collection and structure refinement are given in Table 1.

Differential scanning calorimetry: DSC measurements were performed on a Netzsch DSC 404 C calorimeter from room temperature up to 1573 K with 10 K min^{-1} heating rate. About 50 mg of substance were measured in closed Nb ampoules (∅ 5 mm, 600 mg) under argon atmosphere.

Magnetic susceptibility: A polycrystalline sample of Ba_3Si_4 ($m \approx$ 108 mg) was sealed under He (≈ 400 mbar) in a quartz ampoule and measured in a SQUID magnetometer (MPMS-XL7, Quantum Design) in fields $\mu_0 H$ from 2 mT to 7 T and a temperature range from 1.8 K to 400 K. The contribution of the sample holder was subtracted.

Electrical resistivity: Electrical resistance was measured with a four-point dc method on an irregular crystalline piece (ca. 3.5 × 2.1 ×

Table 2 Atomic coordinates and displacement parameters (in Å^2) for Ba_3Si_4.

Atom	Site	x	y	z	U_{eq}
Ba(1)	4*f*	0.33515(1)	x	0	0.01466(2)
Ba(2)	4*e*	0	0	0.16963(1)	0.01031(1)
Ba(3)	4*d*	0	$^1/_2$	1/4	0.01212(1)
Si(1)	8*i*	0.90055(3)	0.30007(3)	0	0.01134(4)
Si(2)	8*j*	0.20077(3)	x	0.35403(3)	0.01359(5)

Atom	U_{11}	U_{22}	U_{33}	$U_{23} = U_{13}$	U_{12}
Ba(1)	0.01296(2)	U_{11}	0.01805(3)	0	−0.00047(2)
Ba(2)	0.01111(2)	U_{11}	0.00871(2)	0	0.00067(2)
Ba(3)	0.01186(2)	U_{11}	0.01264(3)	0	0
Si(1)	0.01005(9)	0.01263(10)	0.01135(9)	0	−0.00111(8)
Si(2)	0.01303(6)	U_{11}	0.01472(11)	−0.00326(6)	0.00064(8)

U_{eq} is defined as one third of the trace of the orthogonalized U_{ij} tensor, which is exp $(-2\pi^2 [h^2a^{*2}U_{11} + \cdots + 2\,h\,k\,a^*\,b^*\,U_{12}])$

1.7 mm^3). The undefined contact geometry leads to a large inaccuracy (≈ ±50 %) of the absolute resistivity.

NMR: For NMR measurements, fine powder of Ba_3Si_4 was diluted in the volume ratio of about 1:5 with dry GeO_2 (Chempur, 99.999 %) to avoid a skin effect of the electric-conducting material and eddy currents during MAS experiments. The mixture was enclosed under Ar into a ZrO_2 rotor (∅ = 4 mm). The spectra were recorded using a Bruker AVANCE spectrometer (B_0 = 11.74 T, ν = 99.364 MHz for ^{29}Si); MAS and static wide line experiments were performed with a 4 mm standard triple resonance probe (Bruker). The spectral parameters of the MAS signals (ν_{rot} = 2.65 kHz) were determined by a single pulse sequence with 1.5 µs pulse duration. A Hahn-echo pulse sequence with 1.5 µs and 3.0 µs pulse duration and a inter-pulse delay of ν = 60 µs was used for the static measurement. A saturation recovery pulse sequence was used for spin-lattice relaxation (T_1) experiments applying a sample rotation frequency of 7.5 kHz. 30 relaxation delays equally spaced on logarithmic time scale were measured to determine T_1 for each of seven measurement temperatures between 170 K to 298 K. All experiments were performed by eight-fold phase cycling of the pulse sequences. The spectral parameters of the signals were determined from the line shapes by least-squares analysis with the program SIMPSON [11]. The definitions from *Bak* et al. are used for the isotropic signal shift, the anisotropic signal shift and the asymmetry parameter [11]. The signal shifts are referred to tetramethylsilane (TMS).

SEM: The microstructure of the Ba_3Si_4 samples was investigated with a Philips XL 30 Scanning Electron Microscope (LaB_6 cathode). Energy dispersive X-ray spectroscopy (EDXS) was performed with an attached EDAX Si (Li) detector. The composition of nanoporous silicon particles was determined using a high resolution scanning electron microscope, Quanta 200 FEG ESEM (FEI), which was equipped with a Schottky field emission gun (FEG) and an EDAX Si (Li) detector.

TEM: Fine powder of the sample was deposited on a holey-carbon film supported by a copper grid and studied using a Technai 10 electron microscope (FEI).

Calculation procedure

The all-electron full-potential local orbital minimal basis method, FPLO [12], was used in this study. The atomic orbital-like basis functions are obtained by solving an effective Schrödinger equation applying a spherically averaged crystal potential and a confining potential [13]. The confining potential forces the basis functions to be more localized than the genuine atomic orbitals. The presented calculations were performed within the density functional theory [14] in the local density approximation (LDA) [15]. The Perdew-Wang parameterization [16] was chosen for the exchange-correlation potential. The basis sets for Si and Ba consisted of 2*s*, 2*p* / 3*s*, 3*p*, 3*d* and 5*s*, 5*p* / 6*s*, 6*p*, 5*d*, respectively. Convergence with respect to *k* point number was carefully checked. The atomic parameters from single-crystal diffraction data (Tab. 2) were used in the calculations. The electron localization function (ELF) [17, 18] was calculated using a module recently implemented in the FPLO method [19]. Topological analysis of the electron density (ED) and ELF was performed using the program Basin [20].

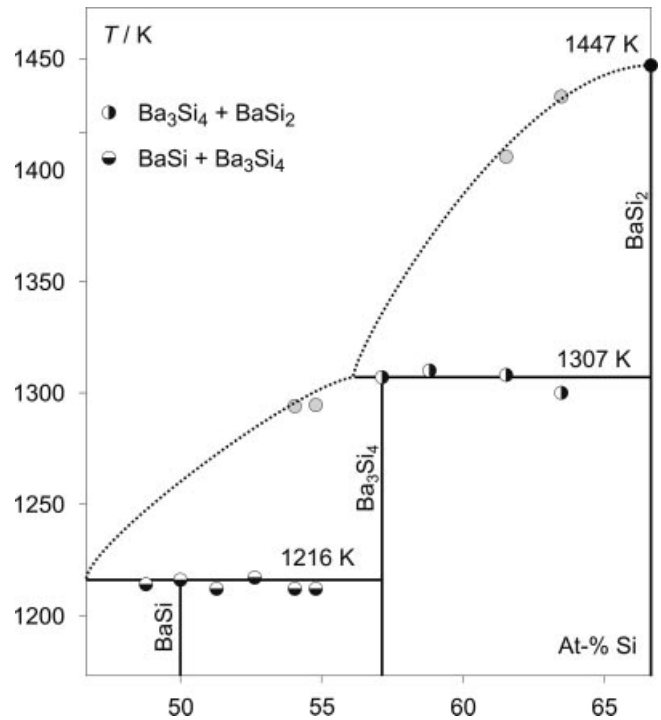

Fig. 2 Phase diagram of the system Ba/Si in the range of 45−67 at-% Si. Grey circles show thermal effects of the liquidus curve. Half-filled circles indicate the phases observed by XRPD (without annealing).

3 Results and Discussion

3.1 Phase relations

In the only former report of the binary system Ba−Si [21], two phases BaSi and $BaSi_2$ were evaluated. Meanwhile, the crystal structures of the phases Ba_2Si [22, 23], Ba_5Si_3 [24, 25], BaSi [26, 27], Ba_3Si_4 [4] and $BaSi_2$ [28−29] are known. Furthermore, Ba_6Si_{25} [30] and $Ba_{8-x}Si_{46}$ [31] have been obtained by high pressure experiments. We reinvestigated the region 45 − 66.7 at-% Si by XRPD, DSC and microstructure analysis. The compositions of the samples and the phase equilibria are shown in Figure 2, the lattice parameters are listed in Table 3. Due to the high sensitivity of

Table 3 Lattice parameters of selected compounds in the system Ba−Si.

Compound	Space group	Lattice parameters in Å	Method	Reference
Ba_3Si_4	$P4_2/mnm$	a = 8.5233(3) c = 11.8322(6)	Powder; Cu $K\alpha_1$ $2\theta_{max}$ = 100°; 115 *hkl* LaB_6 standard	This work
Ba_3Si_4	$P4_2/mnm$	a = 8.5223(4) c = 11.830(1)	Powder; Cr $K\alpha_1$ $2\theta_{max}$ = 100°; 42 *hkl* LaB_6 standard	This work
Ba_3Si_4	$P4_2/mnm$	a = 8.52(2) c = 11.84(2)	Single crystal, Mo $K\alpha_1$	[4]
BaSi	*Cmcm*	a = 5.0404(8) b = 11.937(2) c = 4.1389(7)	Powder; Cu $K\alpha_1$ $2\theta_{max}$ = 100°; 51 *hkl* LaB_6 standard	This work
BaSi	*Cmcm*	a = 5.0430(8) b = 11.933(2) c = 4.1395(8)	Single crystal, Mo $K\alpha_1$	[27]
$BaSi_2$	*Pnma*	a = 8.9314(3) b = 6.7271(2) c = 11.5345(3)	Powder; Cu $K\alpha_1$ $2\theta_{max}$ = 100°; 105 *hkl* LaB_6 standard	This work
$BaSi_2$	*Pnma*	a = 8.92(6) b = 6.75(6) c = 11.57(6)	Single crystal, Mo $K\alpha_1$	[29]

BaSi, Ba_3Si_4 and $BaSi_2$ to oxygen and moisture, and to ensure the equilibrium pressure, DSC measurements were performed in welded Nb crucibles. However, the metal crucibles react rapidly with all silicon containing melts and, therefore, the liquidus line could only be approximated. To investigate, which phases are formed from the melt, the samples were melted by induction heating in open glassy carbon crucibles under Ar and cooled down within few minutes to room temperature.

$BaSi_2$ (66.7 at-% Si) is formed congruently from the melt. The melting point was determined to be 1447(5) K, which is in accordance with the reported phase diagram [21]. Between 57 and 66.7 at-% Si, a mixture of Ba_3Si_4 (57.1 at-% Si) and $BaSi_2$ is always formed after cooling from the melt, indicating a peritectic formation of Ba_3Si_4. The peritectic temperature of Ba_3Si_4 was determined to be 1307(5) K. DSC measurements in Nb ampoules on single-phase samples of Ba_3Si_4 can be misleading, because a sufficient amount of Si reacts always with the Nb crucible, which might give the wrong impression of a congruent instead of a peritectic formation of Ba_3Si_4. Nevertheless, SEM pictures of Ba_3Si_4 samples, which were cooled from the melt within few minutes, show that the phase was directly crystallized from the melt and not formed by diffusion in solid state (Fig. 1). This might also explain why the synthesis of a single phase was only possible in Ta with short annealing times and not in inert glassy carbon crucibles. In the molten state, a part of Si reacts with the crucible wall and therefore Ba_3Si_4 instead of $BaSi_2$ crystallizes from the melt. Towards higher Ba content, Ba_3Si_4 is in equilibrium with BaSi, which decomposes peritectically at 1216(5) K to Ba_3Si_4 and a Ba-rich melt. The lattice parameters of single phase Ba_3Si_4 are identical within e.s.d. with all equilibrium samples in the two-phase regions with $BaSi_2$ and BaSi. Thus the compound exists at a constant composition.

Table 4 Interatomic distances for Ba_3Si_4.

Atoms			d / Å
Ba(1)	− Si(2)	4 ×	3.5761(3)
	− Si(1)	2 ×	3.7017(3)
	− Si(1)	2 ×	3.7163(3)
Ba(2)	− Si(2)	2 ×	3.2584(3)
	− Si(1)	4 ×	3.3598(3)
	− Si(2)	2 ×	3.6177(3)
Ba(3)	− Si(2)	4 ×	3.3088(2)
	− Si(1)	4 ×	3.5174(2)
Si(1)	− Si(1)	1 ×	2.4183(6)
	− Si(2)	2 ×	2.4254(3)
	− Ba(2)	2 ×	3.3598(3)
	− Ba(3)	2 ×	3.5174(2)
	− Ba(1)	1 ×	3.7017(3)
	− Ba(1)	1 ×	3.7163(3)
Si(2)	− Si(1)	2 ×	2.4254(3)
	− Ba(2)	2 ×	3.2584(3)
	− Ba(3)	2 ×	3.3088(2)
	− Ba(1)	2 ×	3.5761(3)

3.2 Crystal structure

The first structure determination [4] resulted in unexpectedly short and different Si−Si bond lengths of about 2.29 Å (1×) and 2.34 Å (4×) in the Si_4^{6-} polyanion (Weißenberg-film data). Assuming an average oxidation number of 1.5− on the silicon atoms [5], the average distance $\bar{d}$ (Si−Si) within the polyanion is expected to be between the average distances in $BaSi_2$ (2.40 Å, Si^{1-}) and BaSi (2.50 Å, Si^{2-}). The previously observed average distance $\bar{d}$ (Si−Si) = 2.33 Å is significantly smaller. The present crystal structure data resolve this discrepancy. In agreement with the previous data, Ba_3Si_4 crystallizes in the space group $P4_2/mnm$ (no. 136) with four formula units in the tetragonal unit cell (Tab. 1−4). Silicon atoms in two crystallographically independent positions form quasi-isolated, butterfly-shaped, Si_4^{6-} anions (Fig. 3a) with the point symmetry $mm2$ − C_{2v} around the position 4*g* (x,$\bar{x}$,0 with x = 0.2505). The bond length between the threefold bonded Si atoms (3b)Si of 2.4183(6) Å is smaller than the distance d((3b)Si − (2b)Si) = 2.4254(3) Å. The differences to the previous data can be understood taking in account that the atomic parameters in [4] were not least-square refined. Now, as expected from the average oxidation number of the silicon atoms in the polyanion, the average bond length $\bar{d}$ (Si−Si) = 2.424(3) Å in Ba_3Si_4 is smaller than in BaSi and larger than in $BaSi_2$ (Tab. 5). The reduction of the tetrahedranide Si_4^{4-} to the Si_4^{6-} anion results in the break of one bond, so that the (2b)Si atoms are now at a distance of 3.4543(6) Å.

The Si_4^{6-} anions are surrounded by 12 Ba cations and each Ba cation by 4 Si_4^{6-} anions: $(Si_4)Ba_{12/4}$. Each Ba atom

Table 5 Average bond lengths and formal charges of the silicon anions.

Compound	Connectivity symbols	Average Si charge	$\bar{d}$ (Si-Si) / Å	Reference
Ba_5Si_3	$(1b)Si^{3-}$, $(0b)Si^{4-}$	− 3.333	2.437(7) 2.74	[25] [24]
BaSi	$(2b)Si^{2-}$	− 2	2.502(3)	[27]
Ba_3Si_4	$(2b)Si^{2-}$, $(3b)Si^{1-}$	− 1.5	2.424(3)	This work
$BaSi_2$	$(3b)Si^{1-}$	− 1	2.404(2)	[48]
$Na_2Ba_6Si_{46}$	$(4b)\ Si^{0.3-}$	− 0.304	2.385(3)	[8]
Si	$(4b)Si^0$	0	2.351776(4)	[58]

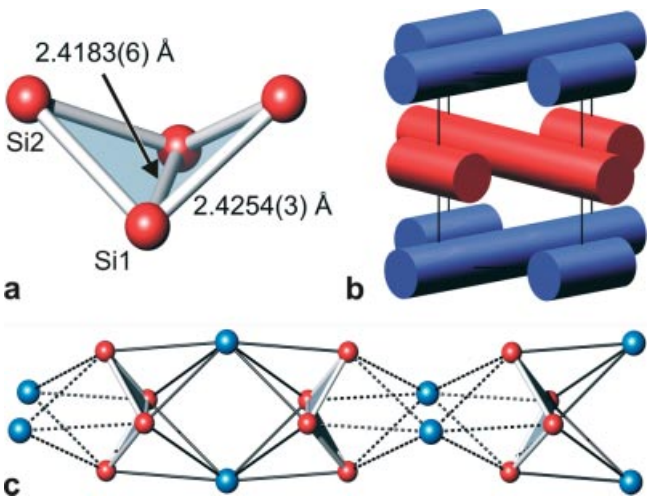

Fig. 3 The Si_4^{6-} anions (**a**) are condensed via Ba atoms to 1D infinite polymers (red and blue) along [110] resulting in a twofold rod packing (**b**, **c**).

is eightfold coordinated by Si atoms. The cations act as single bonded ligands or as μ_2-, and μ_3-bridging ligands. Four μ_3 Ba-bridges of Ba1 and Ba2 complete the Si_4 cluster to a distorted tetrahedron star (*stella quadrangula*), similar to those in K_4Si_4 [32] and Na_4Pb_4 [33]. The Ba1 and Ba2 atoms act as μ_3 bridging ligands for two Si_4 clusters, which results in infinite one dimensional polymers $^1_\infty[Ba_4Si_8]$ along [110]. The polymers form a simple twofold rod packing, in which each neighboring layer is turned by 90° (Fig. 3b, c).

The shortest distance d(Ba1 − Si) = 3.5761(3) Å is much longer than the shortest distances d(Ba2 − Si) = 3.2584(3) Å and d(Ba3 − Si) = 3.3088(2) Å. This may explain that only the Ba2 and Ba3, but not the Ba1 atoms can be substituted by Sr atoms ($Ba_{3-x}Sr_xSi_4$, $0 \le x \le 2$ [34]), and that Sr_3Si_4 does not exist (Fig. 4).

The centers of the $[Si_4]$ clusters at positions $x\bar{x}0$ (x = 1/4) form the non-characteristic Wyckoff position *I*4/*mmm* (2*a*, 2*b*) [35] in the reduced cell $a' = a\sqrt{2}/2$, $c' = c$ and $c'/a' = 1.963$. This leads directly to the Al_3Ti structure-type and to the structures of a series of complex fluorides like $Na_3[UF_7]$, which are hierarchical replacement derivatives [36] of the Al_3Ti type (c/a = 2.01−2.23 for the Al_3Ti members; c/a = 1.97−2.00 for the $Na_3[UF_7]$ members). Figure 5 shows the structures of Al_3Ti and $Ba_3[Si_4]$ with the replacement of Ti (and $[UF_7]$) by the Si_4^{6-} cluster anion.

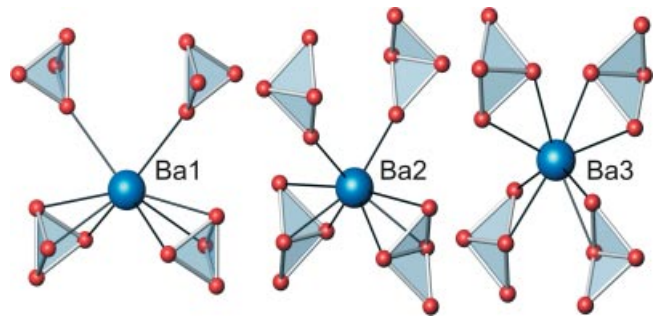

Fig. 4 Coordination of the Ba atoms in Ba_3Si_4 (Si: red spheres).

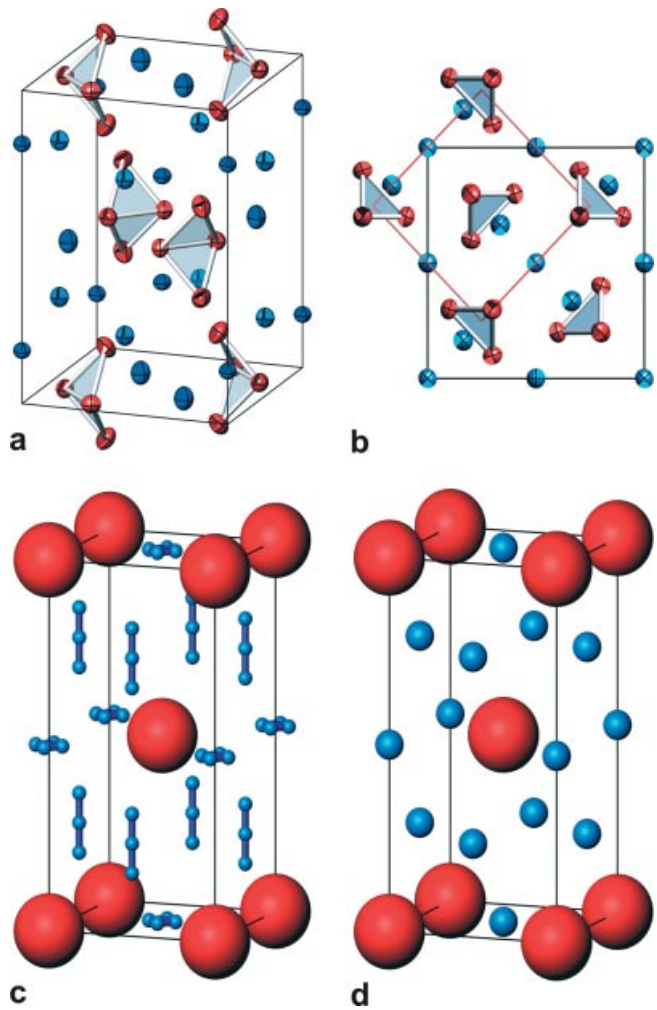

Fig. 5 (**a**, **b**): Unit cell of Ba_3Si_4 with displacement ellipsoids at 99 % probability (Si: red; Ba: blue). The relation to the Al_3Ti structure type is indicated in (**b**) by the smaller red cell in the projection along the c-axis. **c**: Averaged Ba_3Si_4 crystal structure, resulting from the shifts of all equivalent atomic positions into a smaller Al_3Ti segments shown in (**b**). The centers of the Si_4^{6-} anions are represented by large red spheres. **d**: Unit cell of the Al_3Ti structure (Al: blue; Ti: red; $a' = a\sqrt{2}/2$)

Due to the local *mm*2 symmetry of Si_4^{6-}, the Ba cations show small shifts from the ideal Al (or Na) positions.

3.3 Electronic structure

The validity of the Zintl-Klemm concept is sometimes associated with physical property measurements, and especially the metallic state is then believed to be in conflict with the concept. In fact, Zintl phases can be expected to show a low electrical conductivity but they may show metal-like temperature dependence of the conductivity as well. The Zintl-Klemm concept implies an electron transfer to the atoms with the highest electronegativity and this way the covalent bonds of the Zintl anions are derived. The real charges are reduced with ion-to-ion interactions (e.g., $\pm 0.75 - \pm 0.80$ in NaCl [37]), but this does not change the count for the covalent bonds. Applying the concept of 'polar covalency' of *Sanderson* [38], the effective charges in an isolated Ba_3Si_4 molecule are estimated to be $q(Ba) = +1/2$ and $q(Si) = -3/8$. However, detailed predictions for the physical properties can only be obtained from quantum mechanical methods.

The total electronic density of states (DOS) reveals metallic behavior for Ba_3Si_4 with $N(E_F) = 4.8$ states eV^{-1} per cell at Fermi energy (Fig. 6). The states between -3.6 eV and Fermi energy are made up of mainly Si 3*p* and Ba 5*d* basis functions. The occupancies of the Ba 5*d* states ($1.22-1.36\ e^-$) are much larger than those of the 6*s* states ($0.30-0.44\ e^-$) and 6*p* states ($0.26-0.53\ e^-$) and the strong Si 3*p* − Ba 5*d* hybridization is responsible for the non-zero DOS at the Fermi level.

The states forming the Fermi surface can be analyzed from the band structure (Fig. 7). Starting from the Γ−X line, there is one band (red colored) occupied at Γ but unoccupied at X with a large upward dispersion (bandwidth of 0.7 eV). Along the M−Γ line, this band crosses the Fermi energy near Γ, along Γ and Z it becomes unoccupied again close to Z. This band is largely made up of Si(1) p_x, p_y, Ba(2) $d_{x^2-y^2}$ and Ba(3) $d_{3z^2-r^2}$ orbitals. A doubly degenerated band (blue colored) along the Γ−X line is barely unoccupied at Γ with a downward dispersion towards X (bandwidth of ≈ 0.3 eV). This band crosses the Fermi energy between M and Γ close to Γ. Between Γ and Z it stays unoccupied, flat and doubly degenerate and gets occupied again between Z and R close to Z. Major contributors to this band are Si(2) p_z and Ba(1) d_{xz}, d_{yz} orbitals, together with a very weak Ba(3) $d_{3z^2-r^2}$ orbital participation. The topology of the Fermi surface shows no pronounced anisotropy for the metallic conductivity.

A topological analysis of the electron density calculated by FPLO shows that only 3.4 instead of 6 electrons are transferred from the three Ba atoms to the butterfly. Therefore the difference between the total atomic basin charges of the (3b)Si1 atoms (14.7 electrons; $Si^{0.7-}$) and the (2b)Si2 atoms (15 electrons; Si^{1-}) is smaller than expected. Bond distances in Zintl anions are usually related to the charge of the atoms (Table 5) as for the Si_4^{6-} anion *d*(Si1−Si1) is

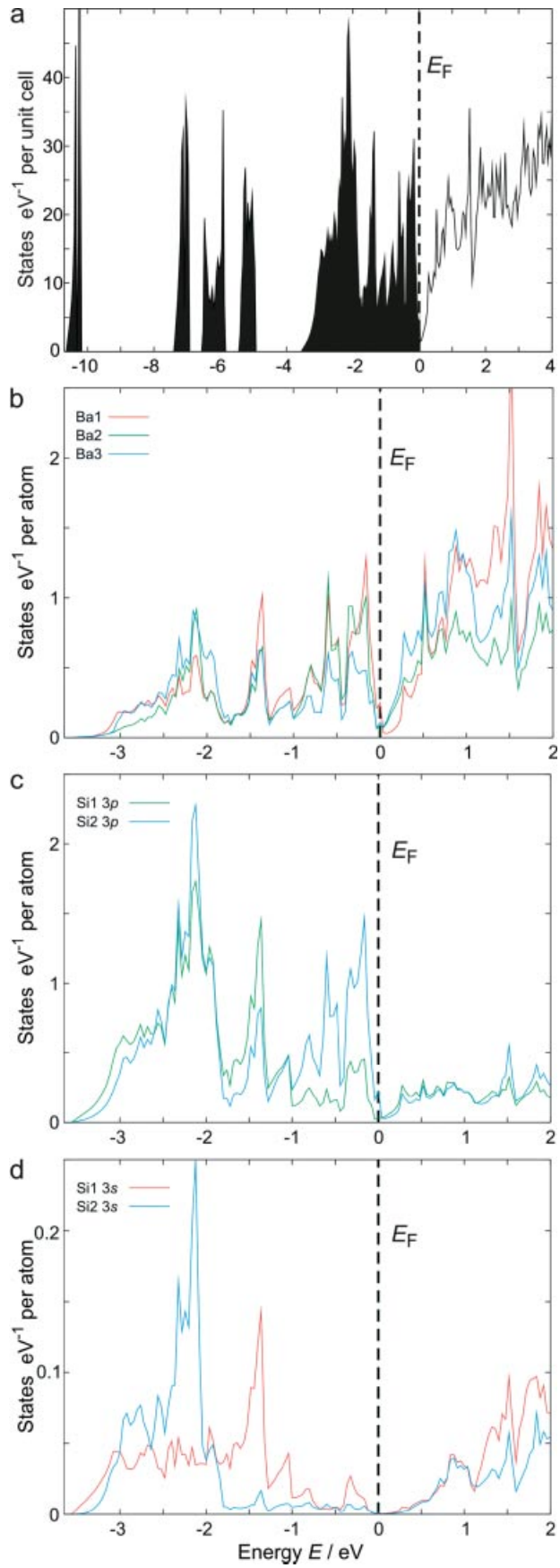

Fig. 6 Total and atom resolved electronic density of states for Ba_3Si_4.

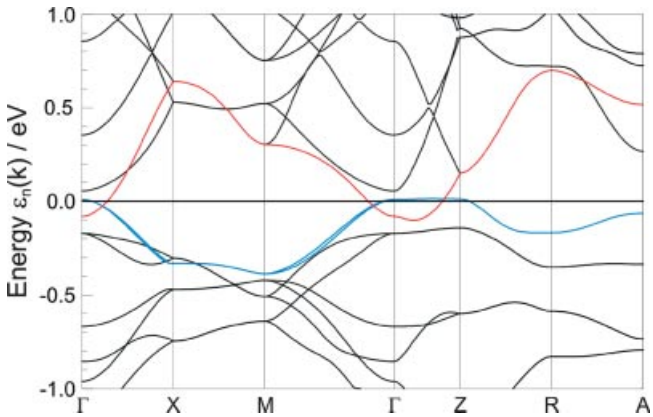

Fig. 7 The electronic band structure between −1 and 1 eV. For colors see text.

smaller than *d*(Si1−Si2). The atomic charges for the Ba atoms with different site symmetries are similar (~54.9 electrons; Ba^{1+}).

Topological analysis of the ELF yields two bond attractors (Si1−Si1, Si1−Si2) and three lone-pair attractors (one for Si1 and two for Si2) in the valence region (Fig. 8). Both bond attractors, Si1−Si1 and Si1−Si2, are off the direct connection line between the Si atoms. With bent Si−Si bonds, the bond angles of the Si atoms become closer to tetrahedral angles, as shown e.g. for carbosilanes [39]. The electron counts in the basins of the Si1−Si1 and Si1−Si2 bonds are 1.0 and 1.6, respectively. The basin of the lone-pair attractor at Si1 contains 2.5 electrons, while the lone pairs at Si2 contain 1.9 and 2.0 electrons. The total electron count of the $(Si1)_2$ fragment is therefore in agreement with the expected value of six electrons, but the distribution between the bond and the lone-pairs is different from the expected one (similar examples were reported by *Chestnut* [40]).

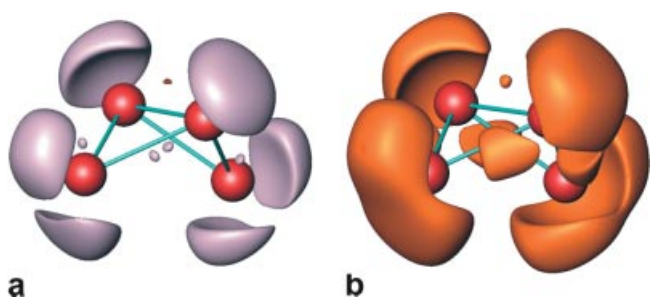

Fig. 8 ELF isosurfaces for the isolated Si_4^{6-} anion. The ELF values are 0.82 for the silver (a), and 0.76 for the golden (b) isosurfaces.

According to the topological analysis of the ELF in the core region, the average of the electron counts in the Ba and Si core basins is 54.4 and 10.1 electrons, respectively. Generally, the individual core shell occupancies as calculated by ELF analysis are never exactly equal to the integer values as required by the *Aufbau* principle, but the total ELF for free atoms are usually within ≈ 0.1 electrons of the corresponding integer value [41]. In Ba_3Si_4, the large deviation of the Ba ELF core basin populations from the expected value of 54.0 is due to the influence of Ba 5*d* orbitals. In the crystalline environment of Ba_3Si_4, the Ba *5d* energy levels go down significantly in energy and become occupied. They contribute to the charge density in the core region, thereby increasing the total ELF core basin population by amounts up to almost half-an-electron.

3.4 Electrical resistivity and magnetism

The temperature-dependent resistivity measurement (Fig. 9) on a polycrystalline bulk sample of Ba_3Si_4 revealed a high resistivity at room temperature but a typical metal-like increase of the resistivity with the temperature (ρ(300 K) ≈ 1.2×10^{-3} Ωm; $\rho_0 \approx 0.4 \times 10^{-3}$ Ωm). Ba_3Si_4 is therefore a "bad metal" with low charge carrier concentration, in agreement with the result of the band structure calculation. A small upturn below 20 K may indicate a metal-to-semiconductor transition.

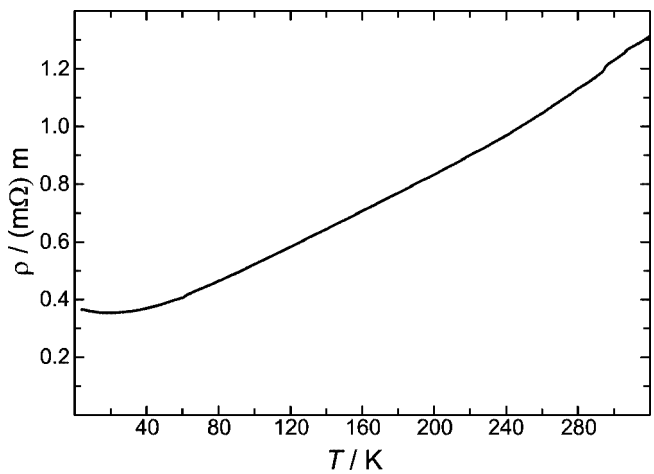

Fig. 9 Electrical resistivity between 3.8 and 320 K.

Magnetization measurements revealed a weakly temperature-dependent diamagnetism of the bulk phase at elevated temperatures with the susceptibility $\chi \approx -50(20) \times 10^{-6}$ $cm^3\ mol^{-1}$ (cgs system) (Fig. 10). With the diamagnetic increments of Ba^{2+} and silicon atoms [42], a distinctly lower susceptibility of about $\chi_{calc} \approx -120 \times 10^{-6}$ $cm^3\ mol^{-1}$ is expected (the value would be even lower for anionic silicon increments). The difference between the measured and calculated values indicates the presence of Pauli paramagnetism. In a free electron model [43] the difference of about 70×10^{-6} $cm^3\ mol^{-1}$ would correspond to a density of states of $N(E_F) \approx 8$ states eV^{-1} per cell, which is on the order of magnitude as the calculated DOS value $N(E_F) =$ 4.8 states eV^{-1} per cell.

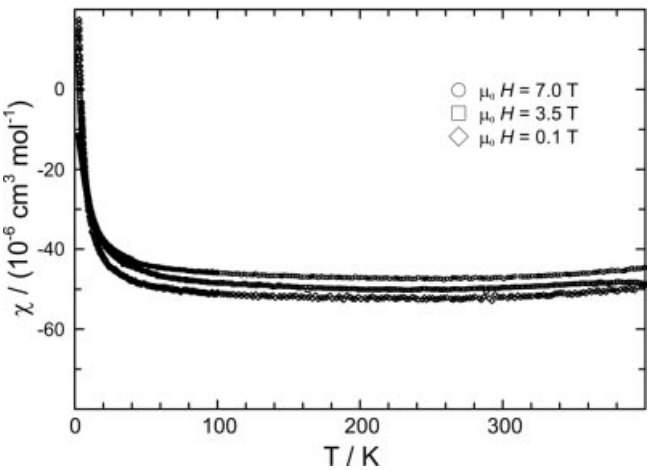

Fig. 10 Magnetic susceptibility between 1.8 and 400 K at μ_0H = 0.1, 3.5 and 7 T.

Below 50 K, the susceptibility rises slightly and in terms of paramagnetic defects this increase would be equivalent to 0.1 % of S = 1/2 species. No superconductivity was found above 1.8 K in fields as low as $\mu_0 H = 2$ mT.

3.5 ^{29}Si *NMR investigations*

The static ^{29}Si NMR experiment on an isotope-enriched Ba_3Si_4 sample showed a broad signal, indicating a superposition of different signal contributions (Fig. 11). Magic angle spinning (MAS) at a low rotation frequency of 2.65 kHz already allowed the separation of two signal contributions (Fig. 11), which is in accordance with two crystallographic sites for the Si atoms (Tab. 2). The spectral parameters (Tab. 6) were determined by a least-squares fit. The isotropic shift positions K_{iso} were confirmed in a series of MAS experiments at different rotation frequencies. The isotropic shift of both ^{29}Si signals is positive and outside of the expected range of -350 ppm $\leq \delta \leq 50$ ppm for diamagnetic, non-metallic materials [44]. The large positive signal shift indicates an interaction of the nuclear spins with the electron spins of conduction electrons (e.g. Knight shift) [45, 46]. For metallic conductors, the isotropic shift of a signal is related to the *s*-orbital contribution of an atom to the density of states at the Fermi energy. Assuming metallic conductivity for Ba_3Si_4, Si1 (0.0005 states eV^{-1} per atom) is assigned to the signal with the lower isotropic shift and Si2 (0.001 states eV^{-1} per atom) to the signal with the higher isotropic shift.

The electrical transport properties of Ba_3Si_4 were investigated with respect to the temperature dependence of the isotropic signal shift (Fig. 12) and of the spin-lattice relaxation times (T_1). The isotropic shift for Si2 is temperature independent, as it is expected for a metal, but the isotropic shift of Si1 slightly increases with temperature, which is frequently observed for semiconductors. A semi logarithmic plot of $K_{iso}/T^{1/2}$ versus T^{-1} shows a positive gradient, which is a clear evidence that Ba_3Si_4 is not a semiconductor (Fig. 13). For semiconductors, a negative gradient is expected [47].

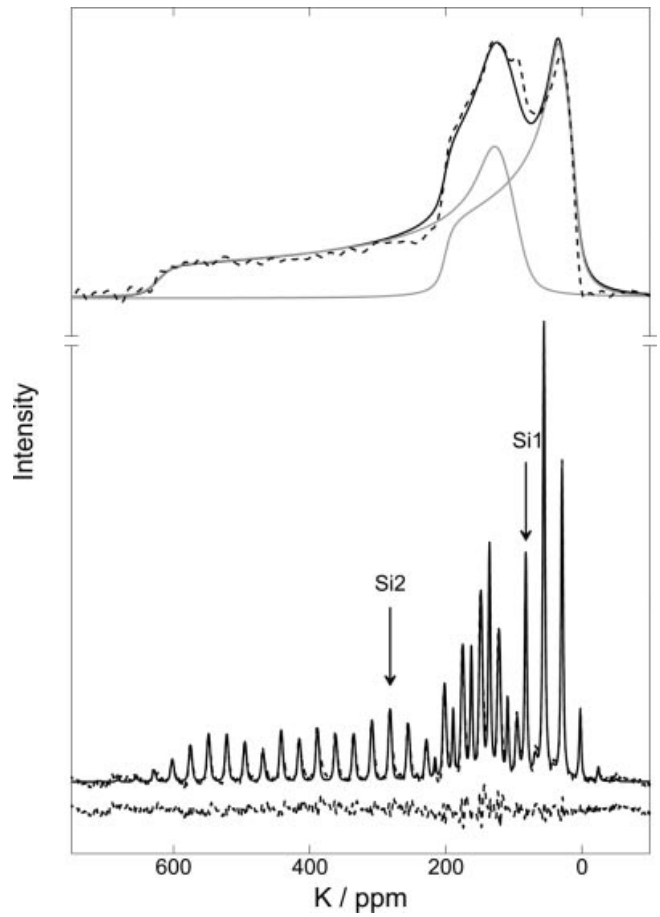

Fig. 11 ^{29}Si NMR signals of enriched Ba_3Si_4. (top) Static experiment; experimental data are represented by a black dashed line. Grey lines represent simulated signal contributions, the black line the sum of the calculated signal conributions. The simulations are based on the spectral parameters obtained by least-squares fitting of the MAS signals. (bottom) Magic angle spinning (MAS) at 2.45 KHz. Full lines represent the sum of the simulated signal contributions, dashed lines the experimental results. The difference between the simulated and experimental signals is shown at the bottom. The simulations of the signals are based on the parameters from Table 6. Isotropic shift positions of the MAS signals are marked by arrows.

Table 6 Spectral parameters of the ^{29}Si NMR signals of enriched Ba_3Si_4 determined by least-squares analysis [11]. K_{iso} corresponds to the isotropic Knight shift, Δ to the anisotropy parameter and η to the asymmetry parameter.

Atoms	K_{iso} / ppm	Δ / ppm	η
Si1	82.4(1)	120.1(3)	0.22(5)
Si2	281.8(1)	348.3(1)	0.10(5)

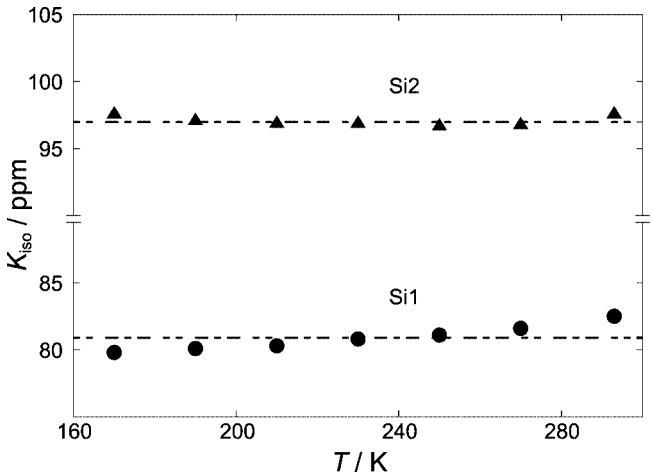

Fig. 12 Isotropic shift of ^{29}Si NMR signals at various temperatures: Si1 (circles), Si2 (triangles), least-squares fit (dotted lines).

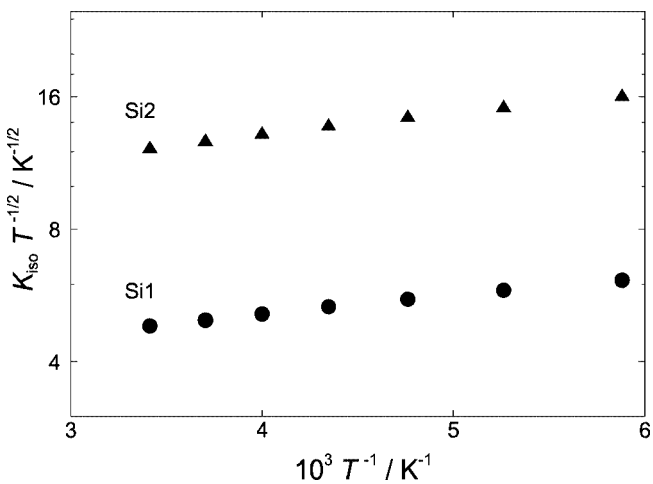

Fig. 13 Semi-logarithmic representation of the ^{29}Si NMR isotropic signal shift $K_{iso}T^{-1/2}$ as a function of T^{-1} (Si1 (circles), Si2 (triangles)).

The spin-lattice relaxation times T_1 differ for both signals. At ambient temperature, the values for Si1 (1.1 s) and Si2 (10.9 s) are large in comparison with well conducting metals, but they are at least two orders of magnitude shorter than observed for the semiconducting alkali metal monosilicides M_4Si_4 (M = Na, K, Rb, Cs) [48]. For semiconductors, a positive gradient of the plot $\log(1/(T_1\ T^2))$ / T^{-1} is expected [47], which is not observed for Ba_3Si_4. In general, T_1 for metals decreases linearly with increasing temperature [45, 46], as it is observed for Si1. T_1 for Si2 shows a non-linear temperature dependence (Fig. 14), indicating another relaxation mechanism, which becomes more relevant at higher temperatures. The reason might be that the charge distribution around Si2 with 2 lone pairs is more anisotropic than for Si1 with 1 lone pair. The higher anisotropy leads to an enhanced spin lattice relaxation, which is due to the interaction of the fluctuating electric field induced by phonons with the charge distribution around the atoms.

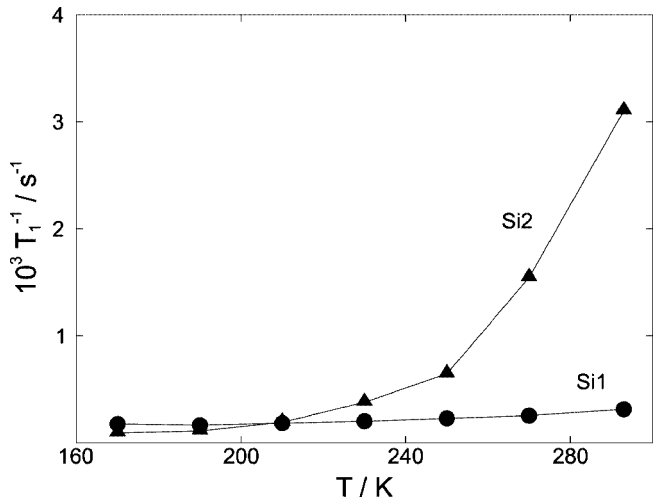

Fig. 14 Spin lattice relaxation times (T1) of the ^{29}Si NMR signals for various temperatures (Si1 (circles), Si2 (triangles)).

The line shape of the signals results from the charge distribution in the vicinity of the Si atoms. The large anisotropy parameter Δ of the signals is due to the chemical shielding, which is caused by orbital contributions of localized electrons. It is about 3 times larger for Si2 than for Si1 (Tab. 6). The anisotropy parameter of Si1 is similar to those observed for the (3b)Si^{1-} anions in M_4Si_4 (M = Na, K, Rb, Cs) [48, 49].

The asymmetry parameter η of the Si2 signal is smaller than that of Si1 (Tab. 6) and they are similar to those observed for Si atoms in M_4Si_4 [48, 49]. An asymmetry parameter different from zero indicates that the symmetry of the charge distribution is reduced compared to an ideal tetrahedranide anion. The charge distribution around the E14 atoms is less distorted for the silicides M_4Si_4 than for the monostannides M_4Sn_4 ($0.26 \leq \eta \leq 0.45$) [50].

3.6 Oxidation of Ba_3Si_4 *with gaseous* HCl

A new application for reactive intermetallic phases has arisen from their oxidation behavior as it was demonstrated by the oxidation of Na_4Ge_4 or $Na_{12}Ge_{17}$ to a new element modification of Ge (*cF*136) [6] or the oxidation of Mg_2Ge to mesoporous Ge [51]. In this work, nanoporous silicon was obtained from the oxidation of Ba_3Si_4 with HCl. Gaseous HCl was evolved from the quantitative dissociation of NH_4Cl into NH_3, N_2, H_2 and HCl at 873 K [52, 53]. Ba_3Si_4 reacted to a fine, brown powder, which is a mixture of nanoporous Si and $BaCl_2$. The reaction is driven by the formation of solid $BaCl_2$. The evolution of gaseous H_2 might suppress the formation of crystalline α-Si and promote the formation of nanoporous Si. The product is stable on air and $BaCl_2$ was removed by water. Similar techniques were previously applied for the syntheses of $Na_{6.2}Si_{46}$ [7], $K_{7.0}Si_{46}$ [7] and $Na_2Ba_6Si_{46}$ [8].

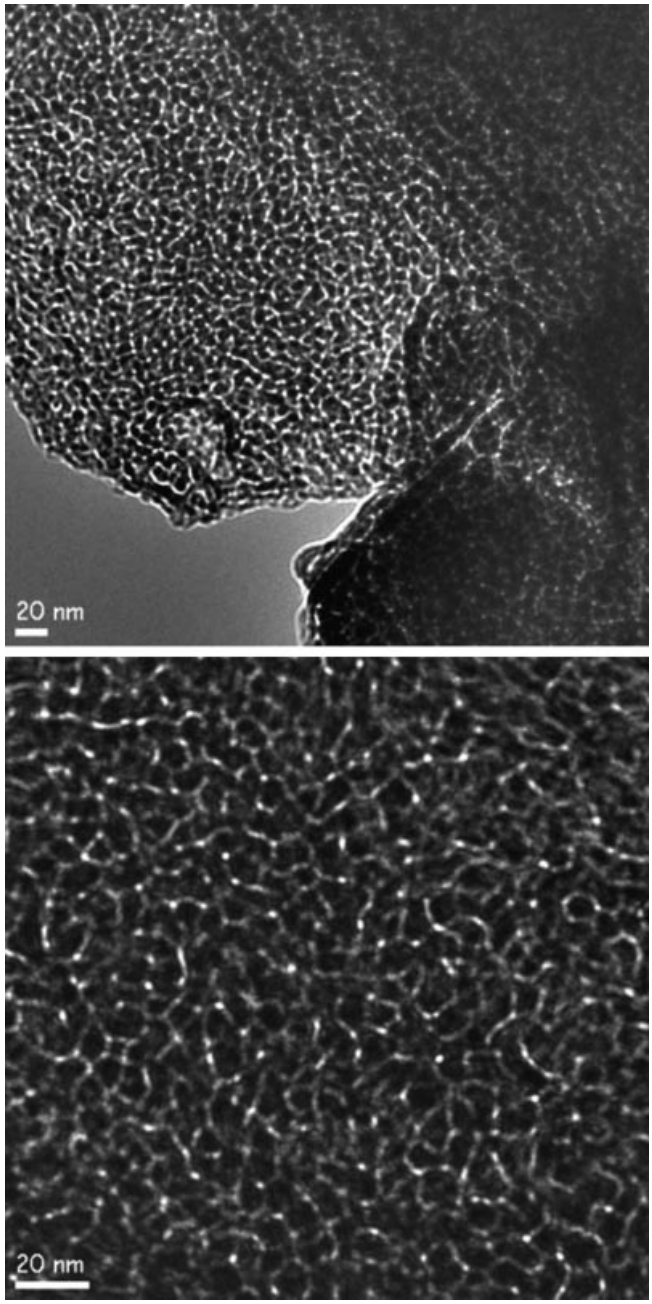

Fig. 15 HREM images of nanoporous Si obtained by oxidation of Ba_3Si_4 with HCl.

HRTEM of the washed sample reveals a porous structure, resembling a sponge, which is amorphous according to the SAED pattern. On average, the cavities have a diameter of about 9 nm and they are not ordered (Fig. 15). Only less than 1 wt-% Ba content was found with EDXS of the bulk sample, while all single particles, which were investigated by high resolution ESEM show only the presence of silicon and a small content of oxygen. Similar reactions were reported with the oxidation of NaSi by NH_4Br to nanocrystalline or amorphous Si particles [54, 55]. These reactions demonstrate the new perspectives for obtaining tailored silicon or germanium morphologies by oxidation of different precursors under adapted reaction conditions. Amorphous silicon is currently used for solar cells, which are easier to manufacture, but less efficient than solar cells based on crystalline silicon.

Remark on Ba_3Ge_4

In our theoretical calculations we find evidence for Ba *5d* contributions to the occupied states both for HT-Ba_3Ge_4, which is isotypic to Ba_3Si_4, and for LT-Ba_3Ge_4 [56]. The DOS, based on FPLO calculations, for HT-Ba_3Ge_4 is very similar to that of Ba_3Si_4 with $N(E_F) = 7.3\ eV^{-1}$ per cell. The DOS of LT-Ba_3Ge_4 is of semi-metallic type with $N(E_F) = 0.7\ eV^{-1}$ per cell. As in the case of Ba_3Si_4, a strong hybridization between Ge 4*p* and Ba 5*d* states is responsible for the (semi-) metallic behavior of both modifications. Contrary to previous results [56] our present TB-LMTO-ASA [57] calculations did not show any band gap for either modification and are in good agreement with the FPLO results.

Weitere Einzelheiten zur Kristallstrukturuntersuchung können beim Fachinformationszentrum Karlsruhe, 76344 Eggenstein-Leopoldshafen (Fax: (+49) 7247-808-666, E-mail@fiz-karlsruhe.de) unter der Hinterlegungsnummer CSD-419308 angefordert werden.

Acknowledgment. The authors would like to thank Dr. S. Hoffmann, P. Scheppan, R. Koban, S. Müller and S. Hückmann for their support and technical assistance.

References

[1] H. G. von Schnering, *Angew. Chem.* **1981**, *93*, 44; *Angew. Chem. Int. Ed. Engl.* **1981**, *10*, 33.
[2] R. Nesper, *Prog. Solid State Chem.* **1990**, *20*, 1.
[3] J. D. Corbett, in: *Chemistry, Structure and Bonding of Zintl Phases and Ions*; S. M. Kauzlarich (Ed.); VCH Publishers, NewYork **1996**, p. 173.
[4] B. Eisenmann, K. H. Janzon, H. Schäfer, A. Weiss, *Z. Naturforsch.* **1969**, *24b*, 457.
[5] H. Schäfer, B. Eisenmann, W. Müller, *Angew. Chem.* **1973**, *85*, 742; *Angew. Chem. Int. Ed. Engl*. **1973**, *12*, 694.
[6] A. M. Guloy, R. Ramlau, Z. Tang, W. Schnelle, M. Baitinger, Yu. Grin, *Nature* **2006**, *443*, 320.
[7] B. Böhme, A. Guloy, Z. Tang, W. Schnelle, U. Burkhardt, M. Baitinger, Yu. Grin, *J. Am. Chem. Soc.* **2007**, *129*, 5348.
[8] B. Böhme, U. Aydemir, A. Ormeci, W. Schnelle, M. Baitinger, Yu. Grin, *Sci. Technol. Adv. Mat.* **2007**, *8*, 410−415.
[9] L. G. Akselrud, P. Y. Zavalii, Yu. Grin, V. K. Pecharsky, B. Baumgartner, E. Wölfel, *Mater. Sci. Forum* **1993**, *133−136*, 335−340.
[10] G. M. Sheldrick, SHELXL-97, Program for Refinement of Crystal Structures, Göttingen **1997**.
[11] M. Bak, J. T. Rasmussen, N. Ch. Nielsen, *J. Magn. Res.* **2000**, *147*, 296.
[12] K. Koepernik, H. Eschrig, *Phys. Rev. B.* **1999**, *59*, 1743.
[13] H. Eschrig, *Optimized LCAO Method and the Electronic Structure of Extended Systems*, Akademie-Verlag and Springer, Berlin 1988.

[14] P. Hohenberg, W. Kohn, *Phys. Rev.* **1964**, *136*, B864.
[15] W. Kohn, L. Sham, *Phys. Rev.* **1965**, *140*, A1133.
[16] J. P. Perdew, Y. Wang, *Phys. Rev. B.* **1992**, *45*, 13244.
[17] A. D. Becke, K. E. Edgecombe, *J. Chem. Phys.* **1990**, *92*, 5397.
[18] M. Kohout, *Int. J. Quantum Chem.* **2004**, *97*, 651.
[19] A. Ormeci, H. Rosner, F. R. Wagner, M. Kohout, Y. Grin, *J. Phys. Chem. A*. **2006**, *110*, 1100.
[20] M. Kohout, Program Basin, ver. 2.42, Dresden, 2007.
[21] I. Obinata, Y. Takeuchi, K. Kurihara, M. Watanabe, *Nippon Kinzoku Gakkaishi*. **1964**, *28*, 568.
[22] A. Widera, H. Schäfer, *Z. Naturforsch.* **1976**, *31b*, 1434.
[23] G. Bruzzone, E. Franceschi, *J. Less-Common Met.* **1978**, *57*, 201.
[24] K. H. Janzon, H. Schäfer, A. Weiss, *Z. Naturforsch.* **1966**, *21b*, 287.
[25] R. Nesper, F. Zürcher, *Z. Kristallogr. NCS* **1999**, *214*, 20.
[26] F. Merlo, M. L. Fornasini, *J. Less-Common Met.* **1967**, *13*, 603.
[27] A. Currao, J. Čurda, R. Nesper, *Z. Anorg. Allg. Chem.* **1996**, *622*, 85.
[28] H. Schäfer, K. H. Janzon, A. Weiss, *Angew. Chem.* **1963**, *75*, 451; *Angew. Chem. Int. Ed. Engl*. **1963**, *2*, 393.
[29] K. H. Janzon, H. Schäfer, A. Weiss, *Z. Anorg. Allg. Chem.* **1970**, *372*, 87.
[30] H. Fukuoka, K. Ueno, S. Yamanaka, *J. Organomet. Chem.* **2000**, *611*, 543.
[31] H. Fukuoka, J. Kiyoto, S. Yamanaka, *Inorg. Chem.* **2003**, *42*, 2933.
[32] H. G. von Schnering, M. Schwarz, J.-H. Chang, K. Peters, E. M. Peters, R. Nesper, *Z. Kristallogr. NCS* **2005**, *220*, 525.
[33] M. Baitinger, K. Peters, M. Somer, W. Carrillo-Cabrera, Y. Grin, R. Kniep, H. G. von Schnering, *Z. Kristallogr. NCS* **1999**, *214*, 455.
[34] U. Aydemir, *unpublished results.*
[35] P. Engel, T. Matsumoto, G. Steinmann, H. Wondratschek, *The Non-characteristic Orbits of the Space Groups, Z. Kristallogr.*, Suppl. Issue Nr. 1, Oldenbourg Verlag, München **1984**.
[36] W. Carrillo-Cabrera, N. Caroca-Canales, H. G. von Schnering, *Z. Anorg. Allg. Chem.* **1994**, *620*, 247.
[37] L. Pauling, *The Nature of the Chemical Bond and the Structure of Molecules and Crystals: An Introduction to Modern Structural Chemistry*. 3th. ed., Cornell University Press, Ithaca, New York 1960.
[38] R. T. Sanderson, *Polar Covalence*, Academic Press, New York 1983.
[39] A. Savin, H. J. Flad, J. Flad, H. Preuss, H. G. von Schnering, *Angew. Chem.* **1992**, *104*, 185; *Angew. Chem. Int. Ed. Engl.* **1992**, *31*, 185.
[40] D. B. Chestnut, *Chem. Phys.* **2001**, *271*, 9.
[41] M. Kohout, A. Savin, *Int. J. Quant. Chem.* **1996**, *60*, 875.
[42] A. Weiss, H. Witte, *Magnetochemie*, Verlag Chemie, Weinheim/Bergstr. 1973, p. 94f.
[43] N. W. Ashcroft, N. D. Mermin, *Solid State Physics*, W. B. Saunders Co., Philadelphia 1976.
[44] J. Mason, *Multinuclear NMR*, Kluwer Academic/Plenum Publishers, New York 1987.
[45] A. Abragam, *Principles of Nuclear Magnetism*, Oxford University Press, New York 1961.
[46] C. P. Slichter, *Principles of Magnetic Resonance*, 3th ed. Springer-Verlag, Berlin, Heidelberg, New York 1990.
[47] H. Selbach, O. Kanert, D. Wolf, *Phys. Rev. B* **1979**, *19*, 4435.
[48] T. Goebel, P. Jeglič, F. Haarmann, *Solid State NMR on Intermetallic Silicides, The 11th European Conference on Solid State Chemistry*, Caen 2007, W70.
[49] D. Mayeri, B. L. Phillips, M. P. Augustine, S. M. Kauzlarich, *Chem. Mater.* **2001**, *13*, 765.
[50] F. Haarmann, D. Grüner, V. Bezugly, H. Rosner, Yu. Grin, *Z. Anorg. Allg. Chem.* **2006**, *632*, 1423.
[51] G. S. Armatas, M. G. Kanatzidis, *Science* **2006**, *313*, 817.
[52] A. Smits, W. de Lange, *J. Chem. Soc.* **1928**, 2944−2952.
[53] H. Oppermann, D. Q. Huong, *Z. Anorg. Allg. Chem.* **1995**, *621*, 665.
[54] P. F. McMillan, J. Gryko, C. Bull, R. Arledge, A. J. Kenyon, B. A. Cressey, *J. Solid State Chem.* **2005**, *178*, 937−949.
[55] X. Zhang, D. Neiner, S. Wang, A. Louie, S. M. Kauzlarich, *Nanotechnology* **2007**, *18*, 1.
[56] F. Zürcher, R. Nesper, *Angew. Chem*. **1998**, *110*, 3451; *Angew. Chem. Int. Ed.* **1998**, *37*, 3314.
[57] O. Jepsen, A. Burkhardt, O. K. Andersen, The Program TB-LMTO-ASA. Version 4.7. Max-Planck-Institut für Festkörperforschung, Stuttgart, **1999**.
[58] NIST Database: **https://srmors.nist.gov/**

